Work published on Signal Processing, 140, pp. 207-218, 2017, DOI 10.1016/j.sigpro.2017.05.021

Effect of Noise and Harmonics on Sine-wave Frequency Estimation by Interpolated DFT Algorithms Based on Few Observed Cycles

Daniel Belega[1] and Dario Petri[2]

[1] Department of Measurements and Optical Electronics, Politehnica University of Timişoara,

Bv. V. Pârvan, Nr. 2, 300223, Timişoara, Romania,

Phone: +40 2 56 40 33 65, Fax : +40 2 56 40 33 62, E-mail: *daniel.belega@upt.ro*

[2] Department of Industrial Engineering, University of Trento,

Via Sommarive, 14-38100, Trento, Italy,

Phone: +39 0461 283902, Fax: +39 0461 281977, E-mail: *dario.petri@unitn.it*

Abstract *— In this paper the performances of two state-of-the-art Interpolated Discrete Fourier Transform (IpDFT) algorithms are analyzed when sine-wave frequency must be estimated over short observation intervals. The first estimator, called enhanced IpDFT (e-IpDFT) algorithm, exploits a two-point interpolation and compensates the detrimental contribution of the fundamental image component on the estimated frequency by using an iterative procedure. The second estimator, called IpDFT-EIF algorithm, eliminates that contribution by using a three-point interpolation. Both algorithms reduce the spectral leakage due to time-domain truncation by weighting the acquired signal by a Maximum Sidelobe Decay (MSD) window. The analysis is performed in the case of ideal, noisy, and noisy and harmonically distorted sine-waves. Theoretical expressions for the estimation Mean Square Errors (MSEs) due to noise and harmonics are derived and verified through simulations and experiments. The performed analysis allows the selection of the best frequency estimator for given signal-to-noise-ratio, harmonic content, and number of acquired cycles.*

Keywords: Discrete Fourier Transform (DFT), error analysis, interpolation, sine-wave frequency estimation, statistical analysis, windowing.

1. Introduction

Sine-waves are used in many applications such as communications, instrumentation, power systems, sonar, and vibration analysis. Either time-domain and frequency-domain approaches have been proposed for accurate measurement of their parameters [1]. Since frequency-domain methods exhibit both good accuracy and low computational burden, they are often preferred to time-domain methods, especially when dealing with real-time applications. One of the most widely adopted frequency-domain approaches is the so-called Interpolated Discrete Fourier Transform (IpDFT) procedure. Indeed, it provides accurate estimates and it is simple to implement [2-11]. To reduce the detrimental contribution on the estimated parameters due to spectral interference from narrow band disturbances like harmonics or spurious tones, the IpDFT procedure weights the analyzed signal by a suitable window function. Cosine class windows are often employed since they are simple to generate and their spectrum can be expressed in closed form. In particular, Maximum Sidelobe Decay (MSD) windows [6, 12] are often adopted since the related IpDFT sine-wave parameter estimates are expressed by simple analytical relationships [2, 5, 6]. Moreover, they exhibit the highest sidelobe decay rate among all the cosine windows with a given number of terms, thus ensuring very good spectral leakage suppression capabilities [12]. Using the IpDFT procedure, at first the sine-wave frequency is estimated by interpolating the two discrete spectrum samples with the largest magnitude [4]. Then, the sine-wave amplitude and phase are determined exploiting the estimated frequency value. As a result, frequency estimation accuracy affects any estimated parameters. One of the main drawbacks of the IpDFT procedure is that a minimum number of sine-wave cycles (usually at least 3 or 4 cycles, depending on the adopted window) needs to be analyzed. Indeed, if very few sine-wave cycles are observed, as occurs for instance when monitoring power grids [8], frequency estimates are heavily affected by the interference from both the fundamental image component and harmonics. An enhanced two-point IpDFT algorithm that exhibits a high rejection to the spectral interference from the image

component has been proposed in [8]. This algorithm, called e-IpDFT frequency estimator in the following, is similar to the one proposed in [9], but the contribution of the fundamental image component on the spectrum samples is removed by using an iterative procedure. It is worth noticing that the accuracy of the e-IpDFT frequency estimator can be improved by using a more accurate phase spectrum model than the one adopted in the literature. Therefore, a modified e-IpDFT algorithm based on such a model will be considered in the following.

Another approach to achieve the same goal exploits multipoint frequency-domain interpolation [13-19]. In particular, a three-point IpDFT algorithm which totally Eliminates the contribution of the spectral Image of the Fundamental component (called in the following IpDFT-EIF frequency estimator) has been proposed in [15] and then recently extended to sine-waves affected by dc-offset [19]. That algorithm provides accurate sine-wave amplitude and phase estimates [17], and outperforms the multi-point IpDFT algorithms based on finite differences of the interpolation points [14, 15].

Due to their capability of suppressing the detrimental contribution of the fundamental image component, the e-IpDFT and IpDFT-EIF procedures are expected to provide accurate frequency estimates when only very few signal cycles are observed. However, in practice the acquired signal is usually affected by harmonics and wideband noise. Unfortunately, to the best of the authors' knowledge, the contribution of such disturbances to the e-IpDFT and IpDFT-EIF frequency estimator accuracies has not been yet analyzed in the scientific literature. To this aim analytical expressions for the Mean Square Errors (MSEs) of the returned frequency estimators are derived in this paper and then verified through both simulation and experimental results.

The performed analysis allows the determination of the minimum number of sine-wave cycles required to ensure a specified IpDFT frequency estimation accuracy. It also enables a rational choice of the best IpDFT frequency estimator for a given application.

The remaining of the paper is organized as follows. In Section 2 the expressions for the MSEs of the e-IpDFT and IpDFT-EIF estimators due to both wideband noise and harmonics are derived. The sensitivity to harmonics and noise of the e-IpDFT and IpDFT-EIF frequency estimator MSEs are analyzed

in Section 3. The e-IpDFT and IpDFT-EIF estimator accuracies are also compared through both computer simulations and experimental results in Section 4. Finally, Section 5 presents some conclusions.

2. MSEs of the e-IpDFT and the IpDFT-EIF frequency estimators

2.1. Theoretical Background

Let us consider the following noisy signal:

$$y(m) = x(m) + e(m) = \sum_{k=1}^{K} A_k \sin\left(2\pi k \frac{f_{in}}{f_s} m + \phi_k\right) + e(m), \quad m = 0,1,2,\ldots,M-1 \tag{1}$$

where $x(\cdot)$ is the harmonically distorted sine-wave, composed by the fundamental component (associated to $k = 1$) and K–1 harmonics, $e(\cdot)$ is an additive white Gaussian noise with zero mean and variance σ^2, and M is the number of acquired samples. In (1) A_k, kf_{in}/f_s, and ϕ_k are the amplitude, the normalized frequency, and the initial phase of the kth harmonic, where f_{in} is the frequency of the continuous-time signal and f_s is the sampling rate. The normalized signal frequency can be expressed as:

$$\frac{f_{in}}{f_s} = \frac{\nu}{M} = \frac{l+\delta}{M}, \tag{2}$$

where $\nu = l + \delta$ is the number of acquired cycles, in which l is the rounded value of ν and $\delta \in$ [-0.5, 0.5) is the inter-bin frequency location. It is worth noticing that non-coherent sampling (i.e. $\delta \neq 0$) often occurs in practice. In (1) K is assumed smaller than $0.5M/\nu$ in order to avoid aliasing.

Observe also that (1) assumes that possible DC offset component has been removed.

To reduce spectral leakage, the samples (1) are weighted by a suitable window $w(\cdot)$ [20]. The Discrete Time Fourier Transform (DTFT) of the windowed signal $y_w(m) = y(m)\cdot w(m)$, $m = 0, 1,\ldots, M-1$ can be expressed as:

$$Y_w(l+r) \stackrel{\Delta}{=} Y_{w(r)} = X_{w(r)} + E_{w(r)} = \sum_{k=1}^{K} \frac{A_k}{2j}\left[W(l+r-k\nu)e^{j\phi_k} - W(l+r+k\nu)e^{-j\phi_k}\right] + E_{w(r)}, \tag{3}$$
$$0 \le l + r < M$$

where $X_{w(\cdot)}$ is the DFT of the weighted harmonically distorted sine-wave $x_w(m) = x(m)\cdot w(m)$, $E_{w(\cdot)}$ is the

DFT of the weighted wideband noise $e_w(m) = e(m)\cdot w(m)$, and $W(\cdot)$ is the DTFT of the window $w(\cdot)$. In (3) r is an integer, which can take the values -1, 0, or 1 when using the e-IpDFT or the IpDFT-EIF algorithms. Moreover, the second term in the square brackets in (3) is related to the image of the kth spectral line.

The IpDFT-EIF and the e-IpDFT algorithms have been proposed for the H-term MSD window, which is expressed by [12]:

$$w(m) = \sum_{h=0}^{H-1} (-1)^h a_h \cos\left(2\pi \frac{h}{M} m\right), \quad m = 0,1,\ldots,M-1 \tag{4}$$

in which [6]: $a_0 = C_{2H-2}^{H-1} / 2^{2H-2}$ and $a_h = C_{2H-2}^{H-h-1} / 2^{2H-3}$, $h = 1,2,\ldots,H-1$, where $C_m^p = p!/[(p-q)!q!]$. The two-term MSD window is also known as the Hann window [12].

When $M >> 1$ and $|\lambda| << M$, the DTFT of the H-term MSD window can be approximated by [6]:

$$W(\lambda) = \frac{M \sin(\pi\lambda)}{2^{2H-2}\pi\lambda} \frac{(2H-2)!}{\prod_{h=1}^{H-1}\left(h^2 - \lambda^2\right)} e^{-j\pi\lambda}, \quad \text{for } |\lambda| << M \tag{5}$$

In the following, the number of acquired signal cycles estimated by the e-IpDFT and the IpDFT-EIF algorithms will be denoted as $\hat{\nu}_{2p} = l + \hat{\delta}_{2p}$ and $\hat{\nu}_{3p} = l + \hat{\delta}_{3p}$, respectively.

2.2. MSE of the e-IpDFT frequency estimator

The e-IpDFT algorithm estimates the sine-wave frequency using a two-step procedure. In the first step, called coarse-search, the spectrum peak location is determined by means of a maximum search procedure applied to the periodogram of the weighted signal $y_w(\cdot)$. When the frequency Signal-to-Noise Ratio is higher than about 17 dB the probability of correct bin selection is very high [5]. The second step, called fine-search, returns the inter-bin frequency location $\hat{\delta}_{2p}$. It interpolates two weighted DFT samples using the iterative procedure proposed in [8] and described in Table 1 using a pseudo-code.

Table 1. Iterative procedure implementing the e-IpDFT frequency estimator.

Step 1: i: = 0

Step 2: estimate the inter-bin frequency location $\hat{\delta}_{2p}^{(0)}$ *by the IpDFT algorithm [2, 5, 6]*

Step 3: estimate the sine-wave amplitude and phase by the IpDFT algorithm [6]

$$\hat{A}_1^{(0)} = 2\frac{\left|Y_{w(0)}\right|}{\left|W(\hat{\delta}_{2p}^{(0)})\right|} \text{ and } \quad \hat{\phi}_1^{(0)} = angle\{Y_{w(0)}\} - \pi\frac{M-1}{M}\hat{\delta}_{2p}^{(0)} - \frac{\pi}{2}sign(\hat{\delta}_{2p}^{(0)}) - angle\left\{W_0(-\hat{\delta}_{2p}^{(0)})\right\},$$

Step 4: i := i + 1

Step 5:compute the ratio:

$$\beta^{(i-1)} = \frac{\left|Y_{w(s)} + \frac{\hat{A}_1^{(i-1)}}{2j}W(2l + s + \hat{\delta}_{2p}^{(i-1)})e^{-j\hat{\phi}_1^{(i-1)}}\right|}{\left|Y_{w(s-1)} + \frac{\hat{A}_1^{(i-1)}}{2j}W(2l - 1 + s + \hat{\delta}_{2p}^{(i-1)})e^{-j\hat{\phi}_1^{(i-1)}}\right|},$$

where s = 0 if $|Y_{w(-1)}| > |Y_{w(1)}|$ *and s = 1 if* $|Y_{w(1)}| > |Y_{w(-1)}|$

Step 6: determine the inter-bin frequency estimate [6]:

$$\hat{\delta}_{2p}^{(i)} = \frac{(H - 1 + s)\beta^{(i-1)} - H + s}{\beta^{(i-1)} + 1}$$

Step 7: determine the sine-wave amplitude and phase estimates:

$$\hat{A}_1^{(i)} = 2\frac{\left|Y_{w(0)} + \frac{\hat{A}_1^{(i-1)}}{2j}W(2l + \hat{\delta}_{2p}^{(i)})e^{-j\hat{\phi}_1^{(i-1)}}\right|}{\left|W(\hat{\delta}_{2p}^{(i)})\right|}$$

and

$$\hat{\phi}_1^{(i)} = angle\{Y_{w(0)} + \frac{\hat{A}_1^{(i-1)}}{2j}W(2l + \hat{\delta}_{2p}^{(i)})e^{-j\hat{\phi}_1^{(i-1)}}\} - \pi\frac{M-1}{M}\hat{\delta}_{2p}^{(i-1)}$$
$$-\frac{\pi}{2}sign(\hat{\delta}_{2p}^{(i-1)}) - angle\left\{W_0(-\hat{\delta}_{2p}^{(i-1)})\right\},$$

Step 8: repeat Steps 4-7 a predefined number I of iterations.

In steps 3 and 7, the function sign(z) represents the sign of its argument z (i.e. it is equal to -1 when $z < 0$ and 1 when $z \geq 0$), and

$$W_0(\lambda)=\sum_{h=0}^{H-1}(-1)^h 0.5a_h\left[\frac{e^{-j\frac{\pi}{M}h}}{\sin\frac{\pi}{M}(\lambda-h)}+\frac{e^{j\frac{\pi}{M}h}}{\sin\frac{\pi}{M}(\lambda+h)}\right]. \tag{6}$$

It is worth noticing that the above phase estimator is more accurate than that used in the classical IpDFT algorithm, in which the approximation $M/(M-1)\cong 1$ is used and the term $angle\left\{W_0(-\hat{\delta})\right\}$ is neglected [5].

The e-IpDFT frequency estimation error can be expressed as:

$$\Delta_{\nu_{2p}}=\hat{\nu}_{2p}-\nu=\Delta_{\nu_{2p,h}}+\Delta_{\nu_{2p,n}}, \tag{7}$$

where $\Delta_{\nu_{2p,h}}$ and $\Delta_{\nu_{2p,n}}$ represent the frequency estimation errors due to harmonics and wideband noise, respectively. Both error components $\Delta_{\nu_{2p,h}}$ and $\Delta_{\nu_{2p,n}}$ can be modeled as statistically independent random variables [7, 15] since they are due to different physical phenomena. Thus, the MSE of the estimator $\hat{\nu}_{2p}$ is given by:

$$MSE[\hat{\nu}_{2p}]=E[\Delta^2_{\nu_{2p}}]=E[\Delta^2_{\nu_{2p,h}}]+E[\Delta^2_{\nu_{2p,n}}], \tag{8}$$

where E[·] represents the expectation operator.

Assuming that the contribution of the spectral image component on the e-IpDFT frequency estimator is negligible, following the same procedure adopted in [7] we obtain:

$$\Delta_{\nu_{2p,h}}\cong(-1)^s\nu\sum_{k=2}^{K}(k-1)\frac{A_k}{A_1}\frac{H+(-1)^s\delta}{\alpha_k+(-1)^s H}\frac{|W(-\alpha_k)|}{|W(-\delta)|}\cos((k-1)\pi\delta+\Delta\phi_k), \tag{9}$$

in which $\alpha_k\overset{\Delta}{=}(k-1)l+k\delta$, $\Delta\phi_k\overset{\Delta}{=}\phi_k-\phi_1$, s = 0 if $|Y_{w(-1)}|>|Y_{w(1)}|$ while s = 1 if $|Y_{w(1)}|>|Y_{w(-1)}|$, and $W(\lambda)$ is given by (5).

Since in practice sampling is incoherent, the initial phases of the fundamental component and harmonics vary randomly in subsequent observation intervals. Thus, they can be modeled as independent uniformly distributed random variables. This implies that the factors $c_k\overset{\Delta}{=}\cos(\Delta\phi_k+\pi(k-1)\delta)$, k = 2, 3,…, K exhibit a U-shaped probability density function (pdf) with zero mean [21], i.e.

$$E[c_k] = E[\cos(\Delta\phi_k + \pi(k-1)\delta)] = 0. \tag{10}$$

Moreover, since the phases are independent it follows that:

$$E[c_k c_l] = E[\cos(\Delta\phi_k + \pi(k-1)\delta)\cos(\Delta\phi_l + \pi(l-1)\delta)] = 0. \tag{11}$$

Conversely when $k = l$ we have:

$$E[c_k^2] = 0.5 + 0.5E[\cos(2\Delta\phi_k + 2\pi(k-1)\delta)] = 0.5. \tag{12}$$

Using (11) and (12), from (9) we easily obtain:

$$E[\Delta^2_{\nu_{2p,h}}] \cong 0.5\nu^2 \sum_{k=2}^{K} \rho^2_{2p}(k), \tag{13}$$

where

$$\rho_{2p}(k) = (k-1)\frac{A_k}{A_1}\frac{H + (-1)^s\delta}{\alpha_k + (-1)^s H}\frac{|W(-\alpha_k)|}{|W(-\delta)|}, \tag{14}$$

whose envelope, which is a decreasing function of ν, represents the maximum contribution of the kth harmonic to the estimated frequency.

Conversely, $E[\Delta^2_{\nu_{2p,n}}]$ is expressed by [6, 7]:

$$E[\Delta^2_{\nu_{2p,n}}] \cong \sigma^2_{\hat{\nu}_{2p}} \cong \frac{(H-|\delta|)^2[2(4H-3)(\delta^2-|\delta|)+2H^2-1]}{(2H-1)^3}\frac{ENBW}{SL^2(\delta)}\frac{1}{M\cdot SNR}, \tag{15}$$

where $SNR \overset{\Delta}{=} A_1^2/(2\sigma^2)$ is the Signal-to-Noise Ratio, while the window Scalloping Loss SL and Equivalent Noise BandWidth $ENBW$ [6, 20] are given by (A.21) and (A.22) reported in the Appendix, respectively.

From (15) it follows that the accuracy of the estimator $\hat{\nu}_{2p}$ increases as ν, M, and SNR increases and H decreases.

By replacing (13) and (15) into (8) we finally achieve:

$$MSE[\hat{\nu}_{2p}] = 0.5\nu^2 \sum_{k=2}^{K} \rho^2_{2p}(k) + \frac{(H-|\delta|)^2[2(4H-3)(\delta^2-|\delta|)+2H^2-1]}{(2H-1)^3}\frac{ENBW}{SL^2(\delta)}\frac{1}{M\cdot SNR}. \tag{16}$$

Expression (16) shows that the sensitivity of the frequency estimator MSE to the normalized power of the kth harmonic, i.e. to A_k^2 / A_1^2 is $c_{2p,h}(k) = 0.5\nu^2 \rho_{2p}^2(k)_{|A_k = A_1}$. Conversely, the estimator MSE sensitivity to the *SNR* related to the wideband noise component is $c_{2p,n} = -\sigma_{\hat{\nu}_{2p}}^2 / SNR$. The values and the behaviors of such sensitivities will be analyzed in Section 3.

2.3. MSE of the IpDFT-EIF frequency estimator

The IpDFT-EIF algorithm estimates the number of acquired signal cycles ν by [16]:

$$\hat{\nu}_{3p} = \sqrt{\mathrm{Re}\{\Pi_1 / \Pi_2\}}, \tag{17}$$

where $\mathrm{Re}\{\cdot\}$ denotes the real operator,

$$\Pi_1 = (2H-1)[(H-l)^2 Y_{w(-1)} + 2(H^2 - l^2 - H)Y_{w(0)} + (H+l)^2 Y_{w(1)}], \tag{18a}$$

and

$$\Pi_2 = (2H-1)(Y_{w(-1)} - 2Y_{w(0)} + Y_{w(1)}). \tag{18b}$$

After some calculations, from (18a) and (18b) it follows that:

$$\hat{\nu}_{3p} = \sqrt{l^2 + \mathrm{Re}\left\{H \frac{(H-2l)Y_{w(-1)} + 2(H-1)Y_{w(0)} + (H+2l)Y_{w(1)}}{Y_{w(-1)} - 2Y_{w(0)} + Y_{w(1)}}\right\}}. \tag{19}$$

Similarly to the e-IpDFT estimator, the frequency estimation error can be expressed as:

$$\Delta_{\nu_{3p}} = \hat{\nu}_{3p} - \nu = \Delta_{\nu_{3p,h}} + \Delta_{\nu_{3p,n}}, \tag{20}$$

where $\Delta_{\nu_{3p,h}}$ and $\Delta_{\nu_{3p,n}}$ are the frequency estimation errors due to harmonics and wideband noise, respectively. Thus we can write:

$$MSE[\hat{\nu}_{3p}] = E[\Delta_{\nu_{3p}}^2] = E[\Delta_{\nu_{3p,h}}^2] + E[\Delta_{\nu_{3p,n}}^2], \tag{21}$$

In (21), using a similar derivation as in Sec. 2.2, we have (see (A.9) in the Appendix):

$$E[\Delta^2_{\nu_{3p,h}}] \cong 0.5\nu^2 \sum_{k=2}^{K} \rho^2_{3p}(k), \tag{22}$$

in which:

$$\rho_{3p}(k) = \frac{k^2-1}{2}\frac{A_k}{A_1}\frac{H^2-\delta^2}{\alpha_k^2-H^2}\frac{|W(-\alpha_k)|}{|W(-\delta)|}, \tag{23}$$

whose envelope, which is a decreasing function of ν, represents the maximum contribution of the kth harmonic to the estimated frequency.

Moreover (see (A.20) in the Appendix):

$$\begin{aligned} E[\Delta^2_{\nu_{3p,n}}] &\cong \sigma^2_{\hat{\nu}_{3p}} \\ &\cong \frac{(H^2-\delta^2)^2}{8H^2(2H-1)^2\nu^2}\Big\{[H^2+\delta(\delta+2l)]^2 + 2[H-\delta(\delta+2l)]^2 + 2H^3(H-2) + 4l^2H^2 \\ &+ 4[H^2-\delta(\delta+2l)][H^2-H+\delta(\delta+2l)]\gamma_1 + [H^2-(\delta+2l)^2](H^2-\delta^2)\gamma_2\Big\} \\ &\times \frac{ENBW}{SL^2(\delta)}\frac{1}{M\cdot SNR}, \end{aligned} \tag{24}$$

In (24) γ_1 and γ_2 represent the correlation coefficients between two DFT spectral samples located one bin or two bins apart, respectively [6, 22-24]. They are given by (A.16) and (A.18) reported in the Appendix. Also, (24) shows that the accuracy of the estimator $\hat{\nu}_{3p}$ increases as ν, M, and SNR increases, as already observed in [18]. It also increases as H decreases.

By replacing (22) and (24) into (21) we finally achieve:

$$\begin{aligned} MSE[\hat{\nu}_{3p}] &\cong 0.5\nu^2 \sum_{k=2}^{K} \rho^2_{3p}(k) \\ &+ \frac{(H^2-\delta^2)^2}{8H^2(2H-1)^2\nu^2}\Big\{[H^2+\delta(\delta+2l)]^2 + 2[H-\delta(\delta+2l)]^2 + 2H^3(H-2) + 4l^2H^2 \\ &+ 4[H^2-\delta(\delta+2l)][H^2-H+\delta(\delta+2l)]\gamma_1 + [H^2-(\delta+2l)^2](H^2-\delta^2)\gamma_2\Big\} \\ &\times \frac{ENBW}{SL^2(\delta)}\frac{1}{M\cdot SNR}. \end{aligned} \tag{25}$$

It is worth noticing that, when $l >> H$, substituting γ_1 and γ_2 with (A.16) and (A.18), respectively, (24) returns the variance of the frequency estimator provided by the three-point IpDFT algorithm, which is [15]:

$$E[\Delta^2_{\nu_{3p,n}}] \cong \sigma^2_{\hat{\nu}_{3p}} \cong \frac{(H^2-\delta^2)^2}{2H^3(2H-1)^3}(4H-3)[(4H-1)\delta^2+H^2]\frac{ENBW}{SL^2(\delta)}\frac{1}{M\cdot SNR}. \tag{26}$$

Expression (26) shows that, when the contribution of the fundamental image component is negligible (i.e. when $l >> H$), the IpDFT-EIF estimator has almost the same accuracy as the three-point IpDFT frequency estimator. Conversely, when that contribution is relevant, the IpDFT-EIF frequency estimator outperforms the classical three-point IpDFT frequency estimator.

Moreover, from (25) it follows that the sensitivity of the frequency estimator MSE to the normalized power of the kth harmonic A_k^2/A_1^2 is $c_{3p,h}(k) = 0.5\nu^2\rho^2_{3p}(k)_{|A_k=A_1}$. Conversely, the estimator MSE sensitivity to the SNR due to wideband noise component is $c_{3p,n} = -\sigma^2_{\hat{\nu}_{3p}}/SNR$. The behaviors of such sensitivities will be analyzed in Section 3.

3. Sensitivity to harmonics and noise of the IpDFT frequency estimator MSEs

According to (14) and (23), the ratio $c_{2p,h}(k)/c_{3p,h}(k)$ between the sensitivities of the e-IpDFT and the IpDFT-EIF frequency estimator MSEs to the normalized power of the kth harmonic is expressed by:

$$\frac{c_{2p,h}(k)}{c_{3p,h}(k)} = \frac{\rho^2_{2p}(k)}{\rho^2_{3p}(k)} = \left[\frac{2}{k+1}\frac{\alpha_k+(-1)^{s+1}H}{H+(-1)^{s+1}\delta}\right]^2. \tag{27}$$

Fig. 1 shows the above ratio for k = 2, 3, and 4 as a function of the number of acquired signal cycles ν when the two-term (Fig. 1(a)) and the three-term (Fig. 1(b)) MSD windows are used. The number of acquired signal cycles ν takes values in the range [1.51, 6) cycles with a step of 1/20. It is worth noticing that at least 1.5 cycles are considered because leakage suppression capabilities of the IpDFT-EIF algorithm prevails for lower values of ν, as it will be shown in the next section. Observe also that a ratio

smaller than one means that the e-IpDFT frequency estimator is less sensitive to the considered harmonic than the IpDFT-EIF estimator.

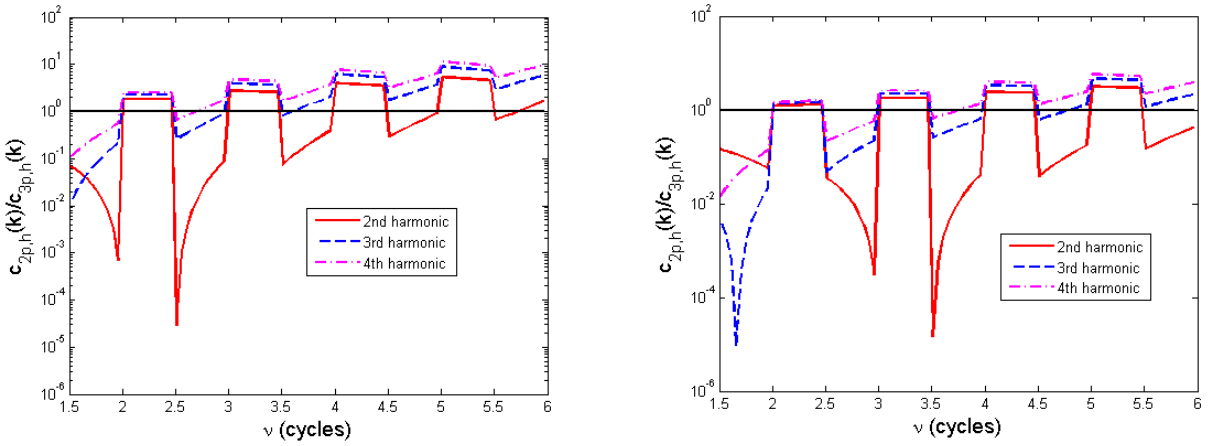

(a) (b)

Fig. 1. The ratio (27) between the MSE sensitivities of the e-IpDFT and the IpDFT-EIF frequency estimators when the sine-wave is affected only by the kth harmonic, k = 2, 3, and 4, versus ν. Two-term (a) and three-term (b) MSD windows.

Fig. 1 shows that both frequency estimators provide accuracies close to each other when the fractional frequency δ is positive (i.e. in the intervals $l < \nu < l + 0.5$, with l integer), although the IpDFT-EIF estimator outperforms the e-IpDFT estimator. Conversely, when δ is negative, the IpDFT-EIF frequency estimator is highly sensitive to harmonics, especially to the 2nd and the 3rd order ones. Moreover, the ratio $c_{2p,h}(k)/c_{3p,h}(k)$ decreases as H increases.

Fig. 2 shows the squares of the maximum contributions to the estimated frequency due to the kth harmonic $\rho_{2p}^2(k)$ and $\rho_{3p}^2(k)$, k = 2 and 3, when assuming $A_k = A_1$, as a function of the number of observed cycles ν. The two-term (Fig. 2(a)) and the three-term (Fig. 2(b)) MSD windows are used.

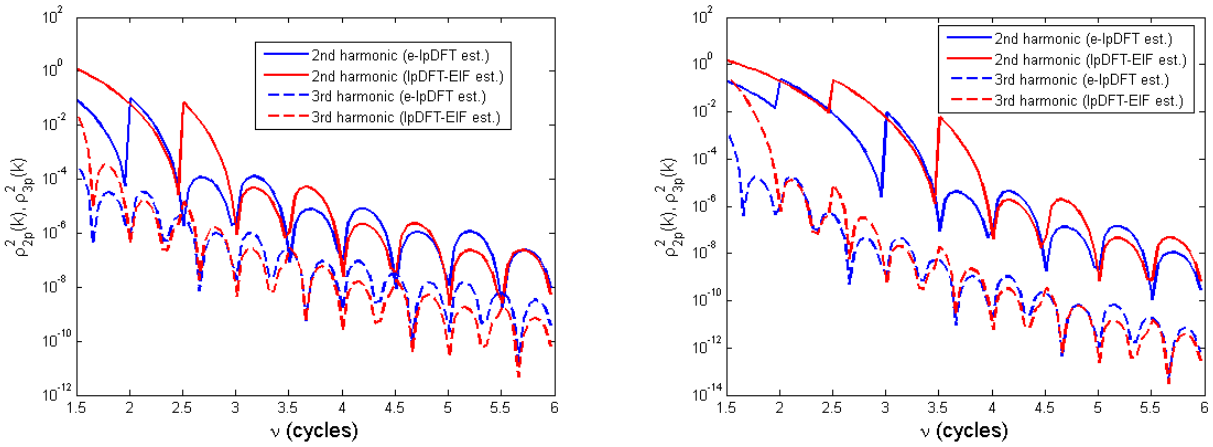

(a) (b)

Fig. 2. Square of the maximum contributions of the *k*th harmonic $\rho_{2p}^2(k)$ and $\rho_{3p}^2(k)$ on the frequency estimates returned by the e-IpDFT and the IpDFT-EIF algorithms versus ν when $A_k = A_1$, $k = 2, 3$. Two-term (a) and three-term (b) MSD windows.

As it can be seen, when the sine-wave is affected by a 2nd harmonic the e-IpDFT estimator outperforms the IpDFT-EIF estimator when $\nu < H + 1$ cycles, except when $2 < \nu < 2.5$ cycles for $H = 2$, and when $2 < \nu < 2.5$ cycles or $3 < \nu < 3.5$ cycles for $H = 3$, where the considered estimator accuracies are close to each other. For the remaining values of ν, the e-IpDFT estimator provides better accuracy in the intervals $l + 0.5 < \nu < l + 1$, l integer (i.e. $-0.5 < \delta < 0$), while the IpDFT-EIF estimator is more accurate when $l < \nu < l + 0.5$ (i.e. $0 < \delta < 0.5$). Conversely, when considering the contribution of a 3rd harmonic the IpDFT-EIF and the e-IpDFT estimators have almost the same accuracy for both $H = 2$ and $H = 3$, except when $\nu < H$ were the e-IpDFT estimator performs better. Moreover, estimators errors of both algorithms are significant when very few cycles are observed, especially when the signal is affected by a 2nd harmonic, even though errors quickly decrease as ν increases.

When the contribution of wideband noise to the estimation error dominates the effect of harmonics, (15) and (24) provide the following expression for the ratio between the sensitivities to noise $c_{2p,n}$ and $c_{3p,n}$ of the e-IpDFT and the IpDFT-EIF frequency estimator MSEs, respectively:

$$\frac{c_{2p,n}}{c_{3p,n}}=\frac{E[\Delta^2_{\nu_{2p,n}}]}{E[\Delta^2_{\nu_{3p,n}}]}\cong\frac{\sigma^2_{\hat{\nu}_{2p}}}{\sigma^2_{\hat{\nu}_{3p}}}\cong\frac{8H^2\nu^2}{2H-1}\frac{2(4H-3)(\delta^2-|\delta|)+2H^2-1}{(H+|\delta|)^2} \tag{28}$$
$$\times\left\{[H^2+\delta(\delta+2l)]^2+2[H^2-\delta(\delta+2l)]^2+2H^3(H-2)+4l^2H^2\right.$$
$$\left.+4[H^2-\delta(\delta+2l)][H^2-H+\delta(\delta+2l)]\gamma_1+[H^2-(\delta+2l)^2](H^2-\delta^2)\gamma_2\right\}^{-1}.$$

Usually that situation occurs when the number of observed cycles ν is much greater than the window order *H*. In that case $E[\Delta^2_{\nu_{3p,n}}]$ is given by (26), and (28) becomes:

$$\frac{c_{2p,n}}{c_{3p,n}}=\frac{E[\Delta^2_{\nu_{2p,n}}]}{E[\Delta^2_{\nu_{3p,n}}]}\cong\frac{\sigma^2_{\hat{\nu}_{2p}}}{\sigma^2_{\hat{\nu}_{3p}}}\cong\frac{2H^3}{(H+|\delta|)^2}\frac{2(4H-3)(\delta^2-|\delta|)+2H^2-1}{(4H-3)[(4H-1)\delta^2+H^2]}. \tag{29}$$

Fig. 3 shows the ratio (28) as a function of the number of observed cycles ν in the range [3, 9) (Fig. 3(a)) and [31, 37) (Fig. 3(b)), for both *H* = 2 and 3. In addition, in Fig. 3(b) the ratio (29) is also reported.

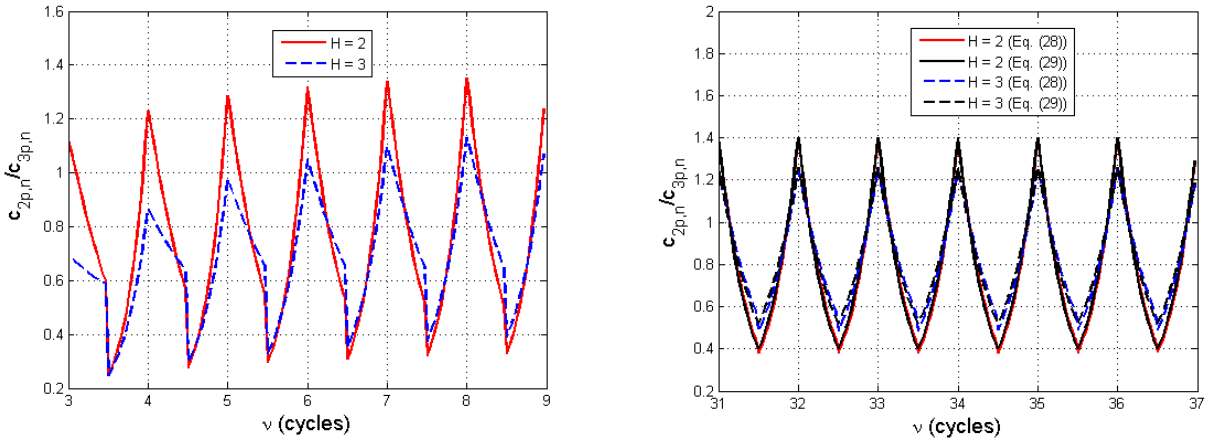

(a) (b)

Fig. 3. Ratio (28) between the MSE sensitivities of the e-IpDFT and the IpDFT-EIF due to wideband noise versus ν in the range [3, 9) cycles (a) and [31, 37) cycles (b). Both two-term (*H* = 2) (a) and three-term (*H* = 3) (b) MSD windows are considered. In figure (b) the values returned by (29) are also reported.

As expected, Fig. 3 shows that the IpDFT-EIF algorithm has a higher sensitivity to wideband noise than the e-IpDFT frequency estimator (i.e. the ratio (28) is smaller than one), except when sampling is

quasi-coherent (i.e. the fractional bin deviation δ is close to 0). Indeed, the sensitivity of IpDFT frequency estimators to wideband noise increases as the number of interpolation points increases [15]. Fig. 3 also shows that the MSE sensitivity ratio slightly decreases as H increases. Moreover, for small values of ν (Fig. 3(a)), the maximum values of the sensitivity ratio slightly increases as ν increases, while it remains almost constant for $\nu > 8$. In addition, for the values of ν considered in Fig. 3(b), (28) and (29) return almost the same results, i.e. the sensitivity ratio is almost independent of l.

4. Computer simulations and experimental results

In this section the accuracies of the e-IpDFT and the IpDTFT-EIF frequency estimators are compared to each other through both computer simulations and experimental results. Only two iterations are considered (i.e. $I = 2$ in Table 1) in the e-IpDFT algorithm since they suffice to almost reach the asymptotic accuracy. The Hann window has been employed in all estimators.

4.1. Simulation results

Simulation runs with $M = 512$ samples were considered. The sine-wave amplitude was $A_1 = 1$, while the number of acquired signal cycles ν was varied in the range (0.5, 6) cycles. For each varying parameter, 1000 runs were generated by choosing at random the phases of each signal component. In the following the accuracies ensured by the considered frequency estimators are compared in the case of pure, noisy, and noisy and harmonically distorted sine-waves.

- ***Pure sine-waves***

Fig. 4 shows the MSE of the e-IpDFT and the IpDFT-EIF frequency estimators as a function of the number of acquired signal cycles ν in the range [0.51, 6) cycles with a step of 0.05 cycles. The input signal is an ideal sine-wave.

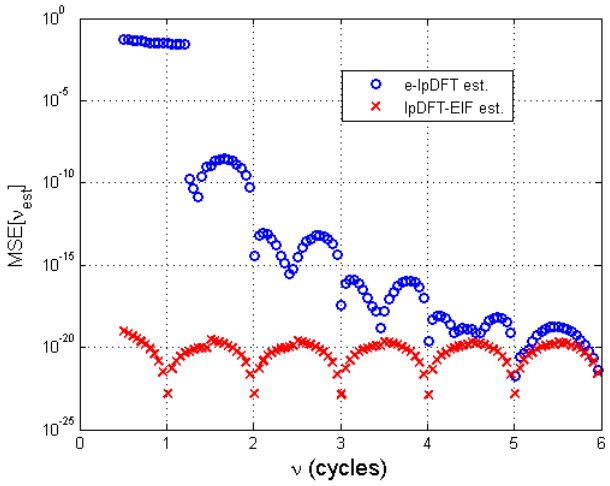

Fig. 4. MSE of the frequency estimates returned by the e-IpDFT and the IpDFT-EIF algorithms based on the Hann window versus ν. Ideal sine-waves.

As it can be seen, the best accuracy is ensured by the IpDFT-EIF frequency estimator. When $0.5 < \nu < 1.5$ cycles the e-IpDFT frequency estimator exhibits poor accuracy. Conversely, the IpDFT-EIF algorithm provides very accurate estimates also when observing less than one cycle. Indeed, when such a low number of cycles is observed, sine-wave amplitude and phase estimates involved in the e-IpDFT algorithm are quite inaccurate due to strong interference from the fundamental image component. The e-IpDFT and the IpDFT-EIF estimators provide a comparable accuracy when at least about 5 cycles are observed. Observe also that the MSE of the IpDFT-EIF estimator essentially depends only on the fractional part of the number of observed cycles δ. This occurs because the IpDFT-EIF algorithm completely removes the effect of the fundamental image component and the residual error is due only to the approximated relationship (5). Conversely, the MSE of the e-IpDFT frequency estimator decreases as ν increases since the related image component rejection capability depends on the accuracies of the other estimated sine-wave parameters, which increases as the number of observed signal cycles increases.

• ***Noisy sine-waves***

Fig. 5 shows the MSEs of the considered frequency estimators returned by both theory (eqs. (15) and (24)) and simulations. It is worth noticing that, under the considered testing conditions, (15) and (24) returns the expressions ($-c_{2p,n}\cdot SNR$) and ($-c_{3p,n}\cdot SNR$), that is they are proportional to the sensitivity to noise of the e-IpDFT and the IpDFT-EIF frequency estimator MSEs, respectively. They are reported as a function of the number of acquired cycles ν when *SNR* = 30 dB (Fig. 5(a)) and *SNR* = 60 dB (Fig. 5(b)). The related single tone CRLB for unbiased estimators, equal to $(\sigma_\nu^2)_{CR} \cong 3/(\pi^2 M \cdot SNR)$ [5], is also reported for comparison. The simulation conditions are the same as in Fig. 4, except that the signal is corrupted by wideband noise.

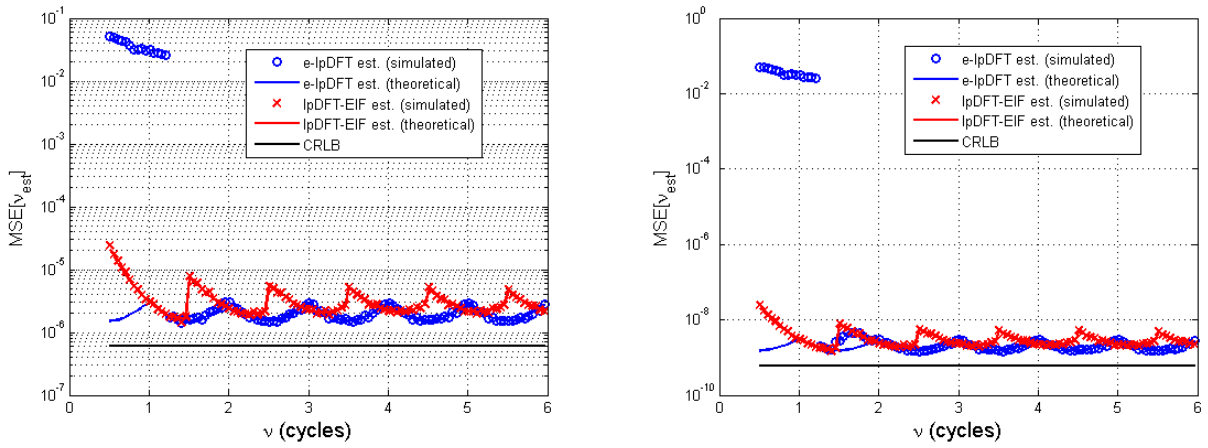

(a) (b)

Fig. 5. MSE of the frequency estimates returned by the e-IpDFTand the IpDFT-EIF algorithms based on the Hann window and the theoretical CRLB versus ν. Noisy sine-waves with *SNR* = 30 dB (a) and *SNR* = 60 dB (b). Values returned by (15) and (24), and simulation results are reported.

When 0.5 < ν < 1.5 cycles, the IpDFT-EIF estimator returns good results while the e-IpDFT estimator exhibits very poor accuracy. That behavior is not explained by theoretical results. Indeed, as Fig. 4 shows, when considering very short intervals, the results returned by the e-IpDFT algorithm are strongly affected by the residual contribution of the image component. Conversely, when ν > 1.5 cycles and *SNR* =

30 dB or $\nu > 2$ cycles and *SNR* = 60 dB, both estimators exhibit a very good agreement between theoretical and simulation results. That behavior occurs because the contribution due to wideband noise largely prevails over the effect of the fundamental image component. In these situations, as expected from theory, the e-IpDFT algorithm outperforms the IpDFT-EIF algorithm, except in quasi-coherent sampling conditions. Also, it can be seen that when $\nu > 1.5$ cycles the maxima of $MSE[\hat{\nu}_{2p}]$ are reached for $\delta = 0$, while those of $MSE[\hat{\nu}_{3p}]$ for δ = -0.5. Moreover, it can observed that the MSEs of all the considered frequency estimators are greater than the CRLB due to windowing [6, 15].

Fig. 6 shows the MSEs of the considered frequency estimators returned by theory (eqs. (15) and (24)) and simulations as a function of *SNR* when $\nu = 1.6$ cycles (Fig. 6(a)) and $\nu = 2.3$ cycles (Fig. 6(b)). The related CRLBs for unbiased estimators are also reported for comparison. The *SNR* was varied in the range [0, 100] dB with a step of 5 dB.

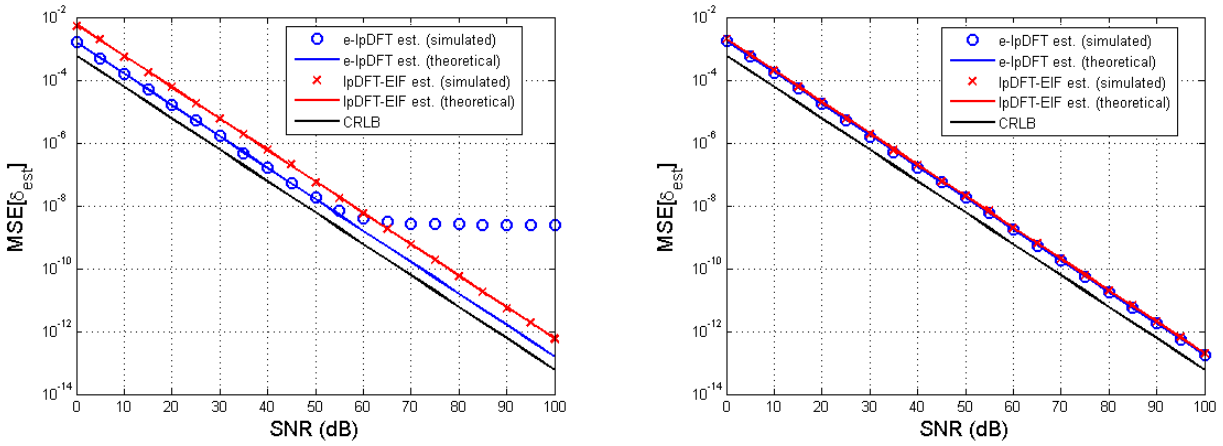

(a) (b)

Fig. 6. MSE of the frequency estimates returned by the e-IpDFT and the IpDFT-EIF algorithms based on the Hann window and the theoretical CRLB versus *SNR*. Noisy sine-waves with $\nu = 1.6$ cycles (a) and $\nu = 2.3$ cycles (b). Values returned by (15) and (24), and simulation results are reported.

As it can be observed the IpDFT-EIF frequency estimator does not suffer from the interference due to the fundamental image component for all the considered values of ν and *SNR*. When $\nu = 1.6$ cycles the

e-IpDFT frequency estimator outperforms the IpDFT-EIF algorithm when *SNR* < 55 dB, while for *SNR* ≥ 65 dB it is heavily affected by the residual effect of the fundamental image component. Conversely, when ν = 2.3 cycles the above detrimental effect is negligible in the whole range of considered *SNR* values. Moreover, the MSEs of both frequency estimators are close to each other.

• ***Noisy and harmonically distorted sine-waves***

Fig. 7 shows the MSEs of the considered frequency estimators returned by both theory (eqs. (16) and (25)) and simulations versus the number of acquired cycles ν when considering a noisy and harmonically distorted sine-wave. The *SNR* equal to 60 dB, while the Total Harmonic Distortion (*THD*), equal to 5%, is due to the 2nd, 3rd, and 4th harmonics with amplitudes in the ratios 4:2:1 (Fig. 7(a)) or 2:4:1 (Fig. 7(b)), respectively. The simulation conditions are the same as in Fig. 4, except that the signal is corrupted by both wideband noise and harmonics. The related single tone CRLB for unbiased estimators is also shown in Fig. 7.

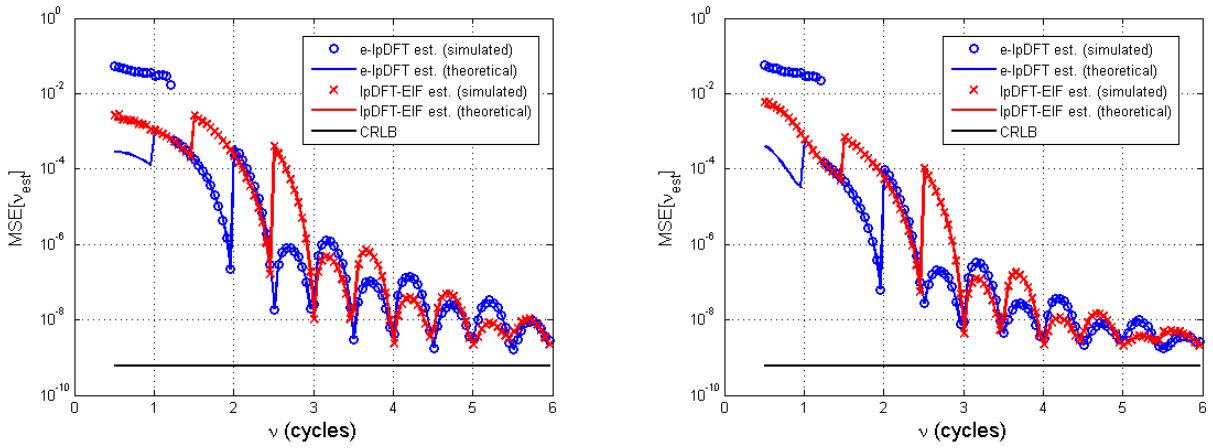

(a) (b)

Fig. 7. MSE of the frequency estimates returned by the e-IpDFT and the IpDFT-EIF algorithms based on the Hann window and the theoretical CRLB versus ν. Noisy and harmonically distorted sine-waves with *SNR* = 60 dB and *THD* = 5% due to 2nd, 3rd, and 4th harmonics, with amplitudes in the ratios 4:2:1 (a) and 2:4:1 (b). Values returned by (16) and (25), and simulation results are reported.

In the considered examples the contribution of harmonics generally prevails over those due to the fundamental image component and wideband noise since their effect on the estimated frequency is not effectively rejected by the algorithms. As expected, Fig. 7 shows that the IpDFT-EIF algorithm outperforms the e-IpDFT algorithm when $0.5 < \nu < 1.5$ cycles. Also, the IpDFT-EIF algorithm MSEs returned by theory and simulations are very close to each other for all considered values of ν, while theory explains the e-IpDFT algorithm MSEs only when $\nu > 1.5$ cycles. When the 2nd harmonic prevails (Fig. 7(a)), the same behavior as in Fig. 2(a) is achieved. Thus, the e-IpDFT frequency estimator outperforms the IpDFT-EIF one for $\nu < 3$ cycles, except when $2 < \nu < 2.5$ cycles, where both estimators exhibit almost the same accuracy. When $3 < \nu < 6$ cycles the e-IpDFT estimator provides better accuracy in the intervals $l + 0.5 < \nu < l + 1$, l integer, while the IpDFT-EIF estimator is more accurate when $l < \nu < l + 0.5$. It is worth noticing that due to the smaller contribution of the 3rd and 4th harmonics behaviors very similar to those reported in Fig. 7(a) are obtained when the signal *THD* is due only a 2nd harmonic of amplitude 0.05. The MSE behavior reported in Fig. 7(b) is the same as in Fig. 7(a), even though the third harmonic overcomes the second one. Indeed, the 2nd harmonic contribution dominates due to its closeness to the fundamental component.

Many other simulations have been performed for different *THD* values. MSE behaviors very similar to those reported in Fig. 7 have been observed as long as the harmonic contribution overcomes the effect of wideband noise. Conversely, when wideband noise prevails, behaviors like those reported in Fig. 5 have been obtained.

4.2. Experimental results

Sine-waves were generated by an Agilent 33220A signal generator, which was used as arbitrary waveform generator through the *Waveform Editor* software. The generated waveforms were acquired by means of an NI6023E acquisition board with sampling rate f_s = 100 kHz and Full Scale Range *FSR* = 10 V. The sine-wave amplitude was set to 2 V and the frequencies were varied in the range [300, 580] Hz

with a step of 20 Hz. Since records of $M = 512$ samples were acquired, the number of analyzed sine-wave cycles varied in the range (1.5, 3.0) cycles. For each frequency value 1000 subsequent runs were analyzed with initial phases varying at random. Three kinds of test signals were considered. The first test signal was a sine-wave with a SIgnal-to-Noise And Distortion ratio *SINAD* of about 52 dB. Noisy and harmonically distorted sine-waves were then obtained by adding to that sine-wave a 2nd, 3rd, and 4th harmonics with amplitudes in the ratios of about 4:2:1 or 2:4:1 and chosen in such a way that the signal *THD* was about 5%. In the case of noisy sine-waves, frequency, and *SINAD* parameters were estimated by means of the four-parameter sine-fit (4PSF) algorithm [26]. When considering noisy and harmonically distorted sine-waves the multi-harmonic sine-fit (MHSF) algorithm was used to estimate frequency, fundamental component and harmonic phases, *SINAD*, and *THD* parameters [27]. Six iterations were performed in both sine-fit algorithms. They were adopted since they provide the maximum likelihood estimators (MLEs) when the input signal is corrupted by additive white Gaussian noise, so ensuring estimator variances very close to the CRLB [28].

Fig. 8 shows the standard deviations of the frequency estimates returned by the e-IpDFT and the IpDFT-EIF algorithms and the square root of the estimated CRLB as a function of the number of analyzed cycles ν in the case of noisy sine-waves. The value of ν was determined as the sample mean of 1000 frequency estimates returned by the 4PSF algorithm. The square root of the CRLB was evaluated by considering the standard deviations of these estimates.

Fig. 8 shows that the e-IpDFT frequency estimator outperforms the IpDFT-EIF algorithm when ν is close to 1.5 cycles and $2 < \nu < 2.7$ cycles. For the remaining values of ν, the IpDFT-EIF frequency estimator outperforms the e-IpDFT frequency estimator. That behavior almost agrees with simulation results reported in Fig. 5. Also, the variances of both analyzed frequency estimators are greater than the related CRLB, mainly due to windowing.

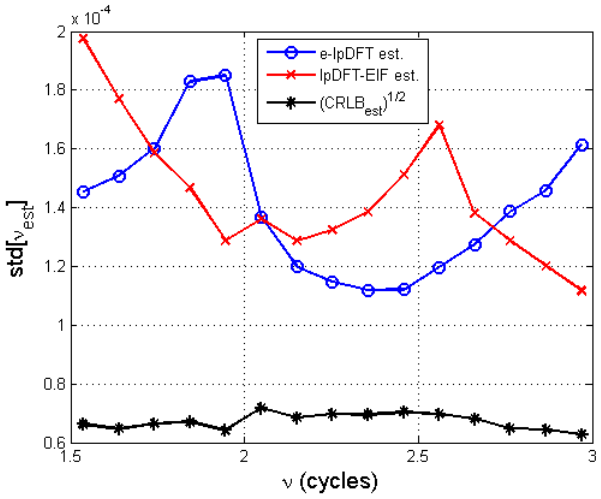

Fig. 8. Standard deviation of the frequency estimates returned by the e-IpDFT and the IpDFT-EIF algorithms based on the Hann window and the estimated square root of the CRLB versus ν. Real noisy sine-waves with *SINAD* ≅ 52 dB. Sine-wave frequency in the range [300, 580] Hz.

Fig. 9 shows the standard deviations of the frequency estimates returned by the considered algorithms and the estimated square root of the CRLB as a function of ν in the case of noisy and harmonically distorted sine-waves. The value of ν was determined as the sample mean of 1000 estimates returned by the MHSF algorithm and the square root of the CRLB was evaluated by considering the standard deviations of these estimates.

Fig. 9 shows that the e-IpDFT frequency estimator outperforms the IpDFT-EIF algorithm in most considered situations, except when $2 < \nu < 2.5$ cycles, where the latter estimator performs slightly better. Also, the standard deviations reported in Fig. 9(b) are smaller than those in Fig. 9(a) due to the smaller amplitude of the 2nd harmonic of the test signal. Moreover, as expected, the variances of both the e-IpDFT and the IpDFT-EIF frequency estimators are higher than the related CRLB even in this case. Observe also that the above results are very similar to those returned by simulations and reported in Fig. 7.

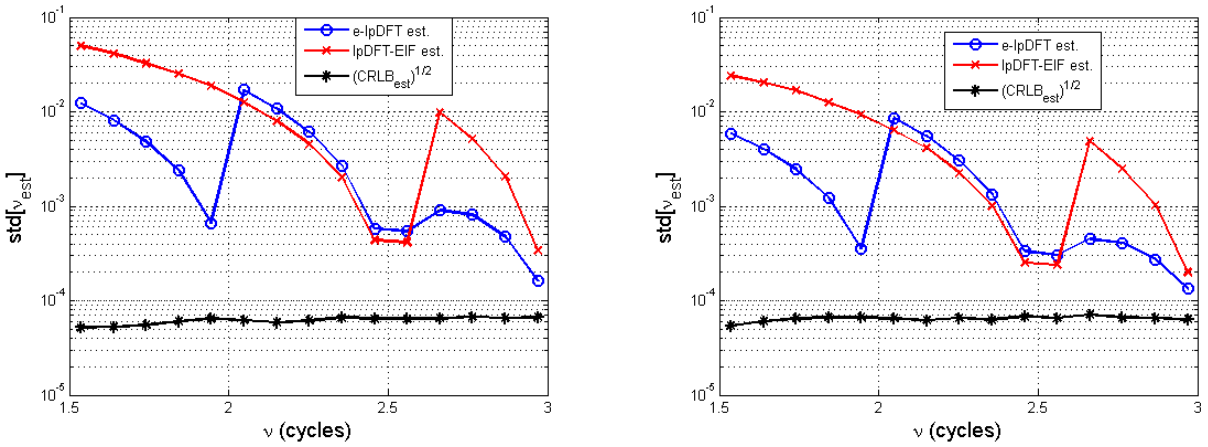

Fig. 9. Standard deviation of the frequency estimates returned by the e-IpDFT and the IpDFT-EIF algorithms based on the Hann window and the estimated square root of the CRLB versus *ν*. Real noisy and harmonically distorted sine-waves with *SINAD* ≅ 52 dB and *THD* ≅ 5%; 2nd, 3rd, and 4th harmonics, with amplitudes in the ratios of about 4:2:1 (a) and 2:4:1 (b). Sine-wave frequency in the range [300, 580] Hz.

4.3. Processing times

The processing times required by the considered frequency estimators when implemented in Matlab 7.1 environment were compared to each other. The DFT was implemented using the defining formula (direct implementation) and the location of the DFT spectrum peak was assumed *a priori* known. The programs were running on a portable computer provided with a 2.6 GHz processor, 4 GB RAM memory, equipped with a Microsoft Windows 8.1 operating system. The average processing times required to obtain 10,000 frequency estimates were 0.27 ms or 0.25 ms when using the e-IpDFT algorithm implemented with two iterations or the IpDFT-EIF algorithm, respectively. Thus, the analyzed frequency estimators require comparable processing efforts.

5. Conclusions

This paper analyzes the accuracies of the e-IpDFT [8] and the IpDFT-EIF [16] frequency estimators through theoretical, simulation, and experimental results in the case when few signal cycles of ideal,

noisy, and noisy and harmonically distorted sine-waves are acquired. Novel analytical expressions for the contribution of both harmonics and wideband noise to the estimator MSEs have been derived. It has been shown that when $0.5 < \nu < 1.5$ signal cycles are observed, the IpDFT-EIF estimator provides a much better accuracy than the e-IpDFT estimator. For $\nu > 1.5$ cycles, when the effect of harmonics prevails over the fundamental image component and wideband noise, the e-IpDFT estimator outperforms the IpDFT-EIF one almost everywhere in the range $1.5 < \nu < 3$ cycles when the fractional part of the observed signal cycles is negative, while the IpDFT-EIF provides slightly better accuracy in the remaining situations. Thus, even though the IpDFT-EIF algorithm eliminates the contribution of the fundamental image component it does not consistently outperform the e-IpDFT algorithm, mainly because the higher number of points used in the frequency-domain interpolation. When the contribution of wideband noise overcomes the effects of the fundamental image component and harmonics, the e-IpDFT frequency estimator outperforms the IpDFT-EIF algorithm, except in quasi-coherent sampling conditions, where the IpDFT-EIF estimator provides better accuracy. It has also been shown that the processing times of both the e-IpDFT algorithm implemented with two iterations and the IpDFT-EIF frequency estimator are very close to each other. The obtained theoretical results have been confirmed through simulation and experimental results.

The MSE expressions derived in this work allow the selection of the best sine-wave frequency estimator among the e-IpDFT and the IpDFT-EIF algorithms when signal-to-noise-ratio, harmonic content and number of acquired signal cycles are given or can be estimated.

Appendix

Derivation of the expression for $MSE[\hat{\nu}_{3p}]$

From (5) the following equalities can be established:

$$W(-1-\alpha_k) = \frac{\alpha_k - H + 1}{\alpha_k + H} W(-\alpha_k), \quad W(1-\alpha_k) = \frac{\alpha_k + H - 1}{\alpha_k - H} W(-\alpha_k), \tag{A.1}$$

where $\alpha_k \overset{\Delta}{=} (k-1)l + k\delta,\ \ k = 1, 2, \ldots, K.$

The contribution due to the harmonic images is negligible as compared to the other terms due to their greater frequency distance from the DFT samples considered by the algorithms. Thus, from (3) and the equalities (A.1) after some algebra we achieve:

$$\begin{aligned} & H(H-2l)Y_{w(-1)} + 2H(H-1)Y_{w(0)} + H(H+2l)Y_{w(1)} \\ & \cong -\frac{A_1}{2j}\frac{2H(2H-1)(\delta^2+2l\delta)}{H^2-\delta^2}W(-\delta)e^{j\phi_1} - \frac{A_1}{2j}\frac{2H(2H-1)(\delta^2+2l\delta)}{(2l+\delta)^2-H^2}W(2l+\delta)e^{-j\phi_1} \\ & + \sum_{k=2}^{K}\frac{A_k}{2j}\frac{2H(2H-1)(\alpha_k^2+2l\alpha_k)}{\alpha_k^2-H^2}W(-\alpha_k)e^{j\phi_k} \\ & + H(H-2l)E_{w(-1)} + 2H(H-1)E_{w(0)} + H(H+2l)E_{w(1)}, \end{aligned} \tag{A.2}$$

and

$$\begin{aligned} Y_{w(-1)} - 2Y_{w(0)} + Y_{w(1)} \cong & -\frac{A_1}{2j}\frac{2H(2H-1)}{H^2-\delta^2}W(-\delta)e^{j\phi_1} - \frac{A_1}{2j}\frac{2H(2H-1)}{(2l+\delta)^2-H^2}W(2l+\delta)e^{-j\phi_1} \\ & + \sum_{k=2}^{K}\frac{A_k}{2j}\frac{2H(2H-1)}{\alpha_k^2-H^2}W(-\alpha_k)e^{j\phi_k} + E_{w(-1)} - 2E_{w(0)} + E_{w(1)}. \end{aligned} \tag{A.3}$$

Since $\left|\sum_{k=2}^{K}\frac{A_k}{A_1}\frac{H^2-\delta^2}{\alpha_k^2-H^2}\frac{W(-\alpha_k)}{W(-\delta)}e^{j\Delta\phi_k} + \frac{W(2l+\delta)}{W(-\delta)}e^{-j2\phi_1} - \frac{E_{w(-1)}-2E_{w(0)}+E_{w(1)}}{jA_1\frac{H(2H-1)}{H^2-\delta^2}W(-\delta)\nu^2 e^{j\phi_1}}\right| << 1,$ where

$\Delta\phi_k \overset{\Delta}{=} \phi_k - \phi_1$, and using the relationship $(1-x)^{-1} \cong 1+x,$ when $|x| << 1$, the ratio between (A.2) and (A.3) becomes:

$$\frac{H(H-2l)Y_{w(-1)}+2H(H-1)Y_{w(0)}+H(H+2l)Y_{w(1)}}{Y_{w(-1)}-2Y_{w(0)}+Y_{w(1)}}\cong$$

$$\left[\delta^2+2l\delta+(\delta^2+2l\delta)\frac{W(2l+\delta)}{W(-\delta)}e^{-j2\phi_1}+\sum_{k=2}^{K}\frac{A_k}{A_1}\frac{H^2-\delta^2}{\alpha_k^2-H^2}(-\alpha_k^2-2l\alpha_k)\frac{W(-\alpha_k)}{W(-\delta)}e^{j\Delta\phi_k}\right.$$

$$\left.+\frac{H(H-2l)E_{w(-1)}+2H(H-1)E_{w(0)}+H(H+2l)E_{w(1)}}{jA_1\dfrac{H(2H-1)}{H^2-\delta^2}W(-\delta)\nu^2e^{j\phi_1}}\right] \tag{A.4}$$

$$\times\left[1-\frac{W(2l+\delta)}{W(-\delta)}e^{-j2\phi_1}+\sum_{k=2}^{K}\frac{A_k}{A_1}\frac{H^2-\delta^2}{\alpha_k^2-H^2}\frac{W(-\alpha_k)}{W(-\delta)}e^{j\Delta\phi_k}-\frac{E_{w(-1)}-2E_{w(0)}+E_{w(1)}}{jA_1\dfrac{H(2H-1)}{H^2-\delta^2}W(-\delta)\nu^2e^{j\phi_1}}\right]$$

$$\cong\delta^2+2l\delta-\sum_{k=2}^{K}(k^2-1)\nu^2\frac{A_k}{A_1}\frac{H^2-\delta^2}{\alpha_k^2-H^2}\frac{W(-\alpha_k)}{W(-\delta)}e^{j\Delta\phi_k}$$

$$+\frac{(H+\delta)(H-\delta-2l)E_{w(-1)}+2(H^2+\delta^2-H+2l\delta)E_{w(0)}+(H-\delta)(H+\delta+2l)E_{w(1)}}{jA_1\dfrac{H(2H-1)}{H^2-\delta^2}W(-\delta)e^{j\phi_1}},$$

where in the last expression only the most significant terms are considered.

By replacing (A.4) in (19) we achieve:

$$\hat{\nu}_{3p}\cong\nu\left(1-\mathrm{Re}\left\{\sum_{k=2}^{K}(k^2-1)\frac{A_k}{A_1}\frac{H^2-\delta^2}{\alpha_k^2-H^2}\frac{W(-\alpha_k)}{W(-\delta)}e^{j\Delta\phi_k}\right\}\right.$$

$$\left.+\mathrm{Re}\left\{\frac{(H+\delta)(H-\delta-2l)E_{w(-1)}+2(H^2+\delta^2-H+2l\delta)E_{w(0)}+(H-\delta)(H+\delta+2l)E_{w(1)}}{jA_1\dfrac{H(2H-1)}{H^2-\delta^2}W(-\delta)\nu^2e^{j\phi_1}}\right\}\right)^{1/2}. \tag{A.5}$$

Remembering that $\sqrt{1+x}\cong 1+x/2$, when $|x|<<1$, we obtain:

$$\Delta_{\nu_{3p}}=\hat{\nu}_{3p}-\nu\cong-\frac{\nu}{2}\mathrm{Re}\left\{\sum_{k=2}^{K}(k^2-1)\frac{A_k}{A_1}\frac{H^2-\delta^2}{\alpha_k^2-H^2}\frac{W(-\alpha_k)}{W(-\delta)}e^{j\Delta\phi_k}\right\} \tag{A.6}$$

$$+\frac{1}{2\nu}\mathrm{Re}\left\{\frac{(H+\delta)(H-\delta-2l)E_{w(-1)}+2(H^2+\delta^2-H+2l\delta)E_{w(0)}+(H-\delta)(H+\delta+2l)E_{w(1)}}{jA_1\dfrac{H(2H-1)}{H^2-\delta^2}W(-\delta)e^{j\phi_1}}\right\}.$$

The first and second term in (A.6) are the frequency estimation errors due to harmonics and wideband noise, respectively, i.e.:

$$\Delta_{\nu_{3p,h}} \cong -\frac{\nu}{2}\mathrm{Re}\left\{\sum_{k=2}^{K}(k^2-1)\frac{A_k}{A_1}\frac{H^2-\delta^2}{\alpha_k^2-H^2}\frac{W(-\alpha_k)}{W(-\delta)}e^{j\Delta\phi_k}\right\}, \tag{A.7}$$

and

$$\Delta_{\nu_{3p,n}} \cong \frac{1}{2\nu}\mathrm{Re}\left\{\frac{(H+\delta)(H-\delta-2l)E_{w(-1)}+2(H^2+\delta^2-H+2l\delta)E_{w(0)}+(H-\delta)(H+\delta+2l)E_{w(1)}}{jA_1\frac{H(2H-1)}{H^2-\delta^2}W(-\delta)e^{j\phi_1}}\right\}. \tag{A.8}$$

Since $E[\cos(\Delta\phi_k+\pi(k-1)\delta)\cos(\Delta\phi_l+\pi(l-1)\delta)]$ is equal to 0.5 when $k = l$ and null otherwise, by applying the expectation operator to $\Delta^2_{\nu_{3p,h}}$ from (A.7) it follows that:

$$E[\Delta^2_{\nu_{3p,h}}] \cong 0.5\nu^2\sum_{k=2}^{K}\rho^2_{3p}(k), \tag{A.9}$$

where

$$\rho_{3p}(k) = \frac{k^2-1}{2}\frac{A_k}{A_1}\frac{H^2-\delta^2}{\alpha_k^2-H^2}\frac{|W(-\alpha_k)|}{|W(-\delta)|}. \tag{A.10}$$

The performed simulations showed that the estimation bias is negligible as compared to the standard deviation as soon as the frequency-domain *SNR* is high enough (e.g. time-domain *SNR* > 0 dB and $M \geq 256$). Thus, by applying the law of uncertainty propagation [25] to (A.8) we achieve:

$$\begin{aligned}E[\Delta^2_{\nu_{3p,n}}] \cong \sigma^2_{\hat{\nu}_{3p}} \cong \frac{(H^2-\delta^2)^2}{4A_1^2H^2(2H-1)^2(l+\delta)^2}\frac{1}{|W(-\delta)|^2}\Big\{&(H+\delta)^2(H-\delta-2l)^2\ \mathrm{var}\left[\mathrm{Re}\{E_{w(-1)}\}\right]\\ &+4(H^2+\delta^2-H+2l\delta)^2\ \mathrm{var}\left[\mathrm{Re}\{E_{w(0)}\}\right]+(H-\delta)^2(H+\delta+2l)^2\ \mathrm{var}\left[\mathrm{Re}\{E_{w(1)}\}\right]\\ &+4(H+\delta)(H-\delta-2l)(H^2+\delta^2-H+2l\delta)std\left[\mathrm{Re}\{E_{w(-1)}\}\right]std\left[\mathrm{Re}\{E_{w(0)}\}\right]corr\left[\mathrm{Re}\{E_{w(-1)}\},\mathrm{Re}\{E_{w(0)}\}\right]\\ &+4(H^2+\delta^2-H+2l\delta)H-\delta)(H+\delta+2l)std\left[\mathrm{Re}\{E_{w(0)}\}\right]std\left[\mathrm{Re}\{E_{w(1)}\}\right]corr\left[\mathrm{Re}\{E_{w(0)}\},\mathrm{Re}\{E_{w(1)}\}\right]\\ &+2(H^2-\delta^2)(H-\delta-2l)(H+\delta+2l)std\left[\mathrm{Re}\{E_{w(-1)}\}\right]std\left[\mathrm{Re}\{E_{w(1)}\}\right]corr\left[\mathrm{Re}\{E_{w(-1)}\},\mathrm{Re}\{E_{w(1)}\}\right]\Big\}.\end{aligned} \tag{A.11}$$

In (A.11):

$$\mathrm{var}\left[\mathrm{Re}\left\{E_{w(-1)}\right\}\right]=\mathrm{var}\left[\mathrm{Re}\left\{E_{w(0)}\right\}\right]=\mathrm{var}\left[\mathrm{Re}\left\{E_{w(1)}\right\}\right]=\sigma_{X_w}^2, \tag{A.12}$$

in which $\sigma_{X_w}^2$ is the variance of the DFT samples, given by [23, 24]:

$$\sigma_{X_w}^2 \cong \frac{M}{2} NNPG\,\sigma^2, \tag{A.13}$$

where *NNPG* is the window Normalized Noise Power Gain [20], given by [6]:

$$NNPG \overset{\Delta}{=} a_0^2 + 0.5\sum_{h=1}^{H-1} a_h^2 = \frac{C_{4H-4}^{2H-2}}{2^{4H-4}}, \tag{A.14}$$

Moreover:

$$corr[\mathrm{Re}\{E_{w(-1)}\}, \mathrm{Re}\{E_{w(0)}\}] = corr[\mathrm{Re}\{E_{w(0)}\}, \mathrm{Re}\{E_{w(1)}\}] = \gamma_1, \tag{A.15}$$

is the correlation coefficient between two DFT spectral samples located one bin apart, given by [6]:

$$\gamma_1 = -\frac{2H-2}{2H-1}, \tag{A.16}$$

while

$$corr[\mathrm{Re}\{E_{w(-1)}\}, \mathrm{Re}\{E_{w(1)}\}] = \gamma_2, \tag{A.17}$$

is the correlation coefficient between two DFT spectral samples located two bins apart, given by [22]:

$$\gamma_2 = \frac{(2H-3)(2H-2)}{2H(2H-1)}. \tag{A.18}$$

It is worth noticing that the correlation coefficient (A.16) is negative since the real-part of $E_{w(-1)}$, $E_{w(0)}$, and $E_{w(1)}$ has alternating signs at adjacent frequency bins.

Using (A.12) – (A.18), after some algebra we obtain:

$$\begin{aligned} E[\Delta_{\nu_{3p,n}}^2] \cong \sigma_{\hat{\nu}_{3p}}^2 \cong \frac{(H^2-\delta^2)^2}{4A_1^2H^2(2H-1)^2\nu^2}\frac{1}{\left|W(\delta)\right|^2}\Big\{&[H^2+\delta(\delta+2l)]^2 + 2[H-\delta(\delta+2l)]^2 \\ &+ 2H^3(H-2) + 4l^2H^2 + 4[H^2-\delta(\delta+2l)][H^2-H+\delta(\delta+2l)]\gamma_1 \\ &+ [H^2-(\delta+2l)^2](H^2-\delta^2)\gamma_2\Big\} M\cdot NNPG\cdot\sigma^2. \end{aligned} \tag{A.19}$$

which can be expressed as:

$$
\begin{aligned}
&E[\Delta^2_{\nu_{3p,n}}] \cong \sigma^2_{\hat{\nu}_{3p}} \\
&\cong \frac{(H^2-\delta^2)^2}{8H^2(2H-1)^2\nu^2}\Big\{[H^2+\delta(\delta+2l)]^2+2[H-\delta(\delta+2l)]^2+2H^3(H-2)+4l^2H^2 \\
&+4[H^2-\delta(\delta+2l)][H^2-H+\delta(\delta+2l)]\gamma_1+[H^2-(\delta+2l)^2](H^2-\delta^2)\gamma_2\Big\} \\
&\times\frac{ENBW}{SL^2(\delta)}\frac{1}{M\cdot SNR}.
\end{aligned}
\tag{A.20}
$$

where:

$$
SL(\delta)\overset{\Delta}{=}\frac{|W(\delta)|}{W(0)}=\frac{\sin(\pi\delta)}{\pi\delta}\frac{[(H-1)!]^2}{\prod_{h=1}^{H-1}(h^2-\delta^2)},
\tag{A.21}
$$

is the window Scalloping Loss (SL) [6, 20],

$$
ENBW\overset{\Delta}{=}\frac{NNPG}{(NPSG)^2}=\frac{C_{4H-4}^{2H-2}}{\left(C_{2H-2}^{H-1}\right)^2},
\tag{A.22}
$$

is the Equivalent Noise BandWidth (ENBW) [6, 20],

$$
NPSG\overset{\Delta}{=}\frac{1}{M}\sum_{m=0}^{M-1}w(m)=\frac{W(0)}{M}=a_0=\frac{C_{2H-2}^{H-1}}{2^{2H-2}}.
\tag{A.23}
$$

is the window Normalized Power Signal Gain [6, 20] and the Signal-to-Noise Ratio (*SNR*) is defined as $SNR\overset{\Delta}{=}A_1^2/(2\sigma^2)$.

References

[1] S.L. Marple, Digital spectral analysis (Prentice-Hall, Englewood Cliffs, 1987).

[2] D.C. Rife, G.A. Vincent, Use of the discrete Fourier transform in the measurement of frequencies and levels of tones, Bell Syst. Tech. J. 49 (1970) 197-228.

[3] B.G. Quinn, Estimation of frequency, amplitude, and phase from the DFT of a time series, IEEE Trans. Signal Process. 45 (3) (1997) 814-817.

[4] C. Offelli, D. Petri, Interpolation techniques for real-time multifrequency analysis, IEEE Trans. Instrum. Meas. 39 (1) (1990) 106-111.

[5] C. Offelli, D. Petri, The influence of windowing on the accuracy of multifrequency signal parameter estimation, IEEE Trans. Instrum. Meas. 41 (2) (1992) 256-261.

[6] D. Belega, D. Dallet, Multifrequency signal analysis by interpolated DFT method with maximum sidelobe decay windows, Meas. 42 (3) (2009) 420-426.

[7] D. Belega, D. Petri, D. Dallet, Impact of harmonics on the interpolated DFT frequency estimator, Mech. Syst. Signal Process. 66-67 (2016) 349-360.

[8] P. Romano, M. Paolone, Enhanced interpolated-DFT for synchrophasor estimation in FPGAs: theory, implementation, and validation of a PMU prototype, IEEE Trans. Instrum. Meas. 63 (12) (2014) 2824-2836.

[9] C. Liguori, A. Paolillo, A. Pignotti, Estimation of signal parameters in the frequency domain in the presence of harmonic interference: a comparative analysis, IEEE Trans. Instrum. Meas. 55 (2) (2006) 562-569.

[10] P. Carbone, E. Nunzi, D. Petri, Frequency-domain-based least-squares estimation of multifrequency signal parameters, IEEE Trans. Instrum. Meas. 49 (3) (2000) 555- 558.

[11] E. Aboutanios, B. Mulgrew, Iterative frequency estimation by interpolation on Fourier coefficients, IEEE Trans. Signal Process. 53(4) (2005) 1237-1241.

[12] A.H. Nuttall, Some windows with very good sidelobe behavior, IEEE Trans. Acoust., Speech, Signal Proces. 29 (1) (1981) 84–91.

[13] C. Candan, A method for fine resolution frequency estimation from three DFT samples, IEEE Signal Process. Lett. 18 (6) (2011) 351-354.

[14] D. Agrež, Dynamic of frequency estimation in the frequency domain, IEEE Trans. Instrum. Meas. 56 (6) (2007) 2111-2118.

[15] D. Belega, D. Dallet, D. Petri, Accuracy of sine-wave frequency estimation by multipoint interpolated DFT approach, IEEE Trans. Instrum. Meas. 59 (11) (2010) 2808-2815.

[16] J. Borkowski, D. Kania, J. Mroczka, Interpolated-DFT-based fast and accurate frequency estimation for the control of power, IEEE Trans. Ind. Electron. 61(12) (2014) 7026-7034.

[17] J. Borkowski, D. Kania, Interpolated DFT-based fast and accurate amplitude and phase estimation for the control of power, Metrol. Meas. Syst. 23(1) (2016) 13-26.

[18] J. Borkowski, D. Kania, J. Mroczka, Influence of the A/D quantization in interpolated-DFT-based system of power control with small delay, Metrol. Meas. Syst. 21(3) (2014) 423-432.

[19] Y. Wang, W. Wei, J. Xiang, Multipoint interpolated DFT for sine waves in short records with dc components, Signal Process. 131 (2017) 161-170.

[20] F.J. Harris, On the use of windows for harmonic analysis with the discrete Fourier transform, Proc. of the IEEE 66 (1) (1978) 51–83.

[21] M.F. Wagdy, W.-M. Ng, Validity of uniform quantization error model for sinusoidal signals without and with dither, IEEE Trans. Instrum. Meas. 38 (3) (1989) 718-722.

[22] D. Belega, D. Petri, Frequency estimation by two- or three-point interpolated Fourier algorithms based on cosine windows, Signal Process. 114 (2015) 115-125.

[23] C. Offelli, D. Petri, Weighting effect on the discrete time Fourier transform of noisy signals, IEEE Trans. Instrum. Meas. 40 (6) (1991) 972-978.

[24] M. Novotný, D. Slepička, M. Sedláček, Uncertainty analysis of the RMS value and phase in frequency domain by noncoherent sampling, IEEE Trans. Instrum. Meas. 56 (3) (2007) 983-989.

[25] Guide for the expression of uncertainty in measurement (GUM), International Organization for Standardization, Switzerland, second edition, 1995.

[26] IEEE Standard for Digitizing Waveform Recorders, IEEE Std. 1057-2007, 2007.

[27] P.M. Ramos, M.F. da Silva, R.C. Martins, A.M. Cruz Serra, Simulation and experimental results of multiharmonic least-squares fitting algorithms applied to periodic signals, IEEE Trans. Instrum. Meas., 55 (2) (2006) 646-651.

[28] S.M. Kay, Fundamentals of Statistical Signal Processing: Estimation Theory (Prentice-Hall, Upper Saddle River, NJ, 1993).